

Collimator-less SPECT System Design for Dynamic Whole-body Imaging

Yuemeng Feng, Arkadiusz Sitek, Abdar Esfahani Shadi, Hamid Sabet*

Abstract—In this study, we introduce a collimator less SPECT system for dynamic whole-body imaging, which enables multi-energy gamma photon detection with higher efficiency compared to mechanically collimated SPECT. The system consists of two detectors, one movable and one fixed, providing a field of view (FOV) adequate for whole-body imaging, while achieving high sensitivity and clinically usable imaging resolution within a reasonable scanning time. This work focuses on the system design using the Monte Carlo simulation toolkit Gate 9.2. The imaging performance is evaluated at two energy peaks (440 keV, 218 keV), representing the major detectable gamma energies generated from Actinium-225, one of the radionuclides under investigation for targeted alpha therapy (TAT). We intend to use the collimator-less system for treatment response monitoring in TAT. Results demonstrate a system resolution of 1.0 cm with a sensitivity of 0.50% for whole-body imaging as measured using a Derenzo-type phantom in the simulation. This demonstrates that the proposed system may serve as an alternative imaging tool for rapid scanning in clinical settings.

Index Terms—whole-body imaging, Compton camera, targeted alpha therapy, SPECT

I. INTRODUCTION

WE evaluate the imaging performance of a Compton scattering-based SPECT system for dynamic whole-body imaging, enabling multi-energy gamma detection with higher efficiency compared to mechanically collimated SPECT. The concept of the Compton camera (CC) for clinical applications was first proposed in the 1970s ([1]). During photon detection, Compton scattering is utilized in Compton cameras, providing them with advantages in multi-energetic gamma imaging. The potential for distinguishing multi-energetic gamma rays, high sensitivity detection, and reduced acquisition time, along with the gantry-free geometry, make CC a competitive non-invasive imaging methodology in clinical ([2]) and pre-clinical settings.

Compton imaging holds particularly value during the process of radiopharmaceutical development ([3]), where each experimental cycle often requires repeated small-animal scans using a PET or SPECT system, depending on the radioisotope used. The goal of employing multi-tracers, which can result in multi-energetic gamma photon emission, is to ensure an accurate measurement of specific target uptake, such as tumor

uptake. While widely used single tracers like ^{18}F -FDG can indicate the specific target uptake, non-specific phenomena contributing to overall target uptake are reported ([4], [5]), potentially leading to false negative observation. Incorporating both a target specific tracer and a non-specific tracer could ensure more accurate detection positions and reduce false discoveries ([5]). However, identifying the optimal multi-tracer for a specific disease is challenging and often requires multiple scans of small animals at low doses. Developing a clinically usable tracer necessitates labeling design, choice of radioisotope, as well as selection of a molecular or ligand, such as an antibody [6]. Mechanical collimation in SPECT offers advantages in multi-isotope imaging ([7]), however, its sensitivity and imaging resolution are lower than PET. The typical resolution is 12-16 mm for whole body SPECT applications ([8]), while PET has a 10 mmm resolution. PET provides better sensitivity than SPECT systems, but its detectable gamma rays are limited to two opposite gamma photons at 511 keV. Although PET is routinely used for small animal imaging, one drawback is its higher cost compared to SPECT. While SPECT has demonstrated several advantages in pre-clinical tracer design ([5, 9]), it is important to note that when gamma energy exceeds several hundred keV, imaging resolution may be compromised due to Compton scattering. The utilization of Compton-scattered photons for dose distribution imaging presents an appealing option. If the detector's energy resolution meets the necessary requirements, this approach can provide both pre-clinically usable imaging resolution and high sensitivity simultaneously.

The feasibility of in vivo human imaging using a Compton system has been demonstrated in [10] where ^{99m}Tc -DMSA and ^{18}F -FDG are utilized, two of the most widely used tracer in SPECT imaging and PET imaging. Evidence has shown that Compton camera is capable of imaging these two tracers at clinical dose level. Benefitting from the collimator-free feature, a Compton scattering based prototype for imaging-guided surgery is proposed in [11]. Furthermore, a hybrid Compton PET system is proposed in [12], with experimental outcomes showing successful detection of multi-gamma ray accumulation in multiple organs for small animal imaging. While there is evidence demonstrating achievable Compton imaging resolution for multi-energetic gamma imaging in small animals, there is currently no conclusive evidence regarding the potential imaging resolution attainable with Compton camera imaging for whole-body human imaging. Several research efforts have

The authors are with Department of Radiology, Massachusetts General Hospital, Harvard Medical School (e-mail: yfeng16, asitek, abdaresfahani.shadi, hsabet@mgh.harvard.edu).

> REPLACE THIS LINE WITH YOUR MANUSCRIPT ID NUMBER (DOUBLE-CLICK HERE TO EDIT) <

been ongoing to enhance the imaging quality of Compton imaging. These include system geometry design ([2, 3]), and accurate modeling in reconstruction ([13, 14]). Unlike the linear projection employed in PET and SPECT system, CC reconstruction is based on Compton conical projection, where angular uncertainties are crucial for evaluating the imaging resolution. Consequently, both the detector intrinsic resolution and detector energy resolution should be considered in the system design, given that the Compton cone is defined by photon energies and the interaction locations.

Apart from its application for multi-tracer in pre-clinical and clinical imaging, CC imaging can serve as a tool for treatment monitoring during the targeted radionuclide therapy (TRT). TRT has been proposed for cancer treatment over the past decades and has gained growing interest in clinical studies following the success of FDA-approved radionuclide: ^{223}Ra dichloride ([15, 16]). Among the on-going studies, two types of radiation emitters are under investigation: alpha and beta particles. Alpha emitters are considered better candidates than beta emitters due to their more efficient killing of malignant cells and less damage to normal tissue ([16]). With the increasing development of TAT for cancer treatment, several radionuclides such as Actinium-225 (^{225}Ac), Bismuth-213 (^{213}Bi), Astatine-211 (^{211}At), and Lead-212 (^{212}Pb), combined with antibodies or small molecules, are being investigated in clinical trials. Over the past decades, ^{225}Ac has been used to treat various types of cancer, and ongoing clinical trials continue to assess its dose tolerance and toxicity [17]. During the decay of ^{225}Ac , alpha daughters such as ^{221}Fr (11.6% emission probability) and ^{213}Bi (26.1 % emission probability) are generated, which then decay emitting 218 keV photons and 440 keV photons detectable by gamma cameras ([18]). We have summarized several clinical cases in Table 1, where the tolerated dose level varies from 30 MBq per patient to 1.5 $\mu\text{Ci}/\text{kg}$. Depending on the patient's weight, the administered dose might vary, for ^{225}Ac the typical administered dose is 2 mCi (74 MBq) as summarized in [17]).

TABLE I

^{225}Ac DOSE LEVEL IN THE TREATMENT OF CANCER

Setting	Dose
Neuroendocrine tumors	5.5 MBq-7 MBq [19, 20]
glioblastoma	10, 20, 30 MBq [21]
Prostate cancer	100 kBq/kg-50 kBq/kg [22]
Small cell lung cancer	120 kBq/kg [17]
Acute myeloid leukemia	0.074-0.0555 kBq/kg [23]

The emission of multi-energetic gamma photons during the decay of alpha daughters necessitates multi-energetic gamma imaging for quality control during treatment and the developmental phase ([9]). Compton camera ([2, 3]) as well as the combination of Compton and PET imaging ([12, 24, 25]), as alternative options to mechanical collimated SPECT have gained increasing attention. For the current state, limited

approaches have been proposed for mechanical collimated SPECT in TAT imaging. A study has demonstrated the possibility of quantitative SPECT imaging for alpha agents ([26]) with three state-of-the-art SPECT/CT system (GE discovery NM/CT 670, GE Optima NM/CT 640, Siemens Symbia T6). However, due to the low gamma counts, the spheres smaller than 1.3 cm in the tested NEMA phantom are not visible with 53 kBq/mL of ^{225}Ac injected. Therefore, only the largest (3.7 cm) and second largest (2.2 cm) spheres are used for quantitation. Enhancing sensitivity through the utilization of a collimator less SPECT system could potentially address the issue of low detected counts. Although Compton systems hold significant promises for small animal imaging, our work focuses on a collimator-less SPECT system designed for dynamic human whole-body imaging. We systematically assess various geometry parameters, including scatterer and absorber thickness, distance from the scatterer to the absorber, and spatial resolution of detectors. We employ the reconstructed image resolution as key metric for imaging system performance. The objective is to determine the optimal geometry parameters for each detector that yield optimal performance. With these optimized geometry parameters, we proceed to evaluate the collimator-less SPECT system designed for human body imaging. The proposed imaging system consists of two detector heads: one fixed opposite the patient bed, and the other parallel to the patient's side, movable in three dimensions to ensure both high sensitivity and clinically applicable imaging resolution. We intend to develop a device to facilitate treatment monitoring during targeted alpha therapy by imaging the gamma rays emitted during the daughter production of the treatment compound. Additionally, a single detector within the system can also be utilized for radio-pharmaceutical development by performing small animal scans.

This paper explores the feasibility of utilizing a Compton camera for whole-body imaging in the context of TAT. To achieve this, we first measure the achievable imaging resolution by simulating a Derenzo phantom using the Gate Monte Carlo simulation toolkit. Section 2 presents the simulation setting of the phantom, the different geometry parameters simulated for detector design and the two-detector system. The reconstructed resolution of the two-detector system across various locations within the FOV is presented in section 3. We discuss the current performance of the imaging system and summarize both its limitations and advantages in section 4. Lastly, we provide insights into the practicality and effectiveness of our current design for whole body imaging in TAT in section 5.

II. METHODS

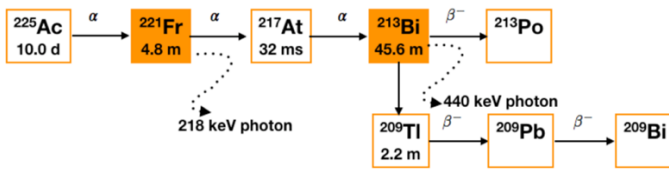
We evaluated the imaging performance of the collimator-less SPECT system for whole-body imaging by simulating a source of ^{225}Ac . All the data presented are simulated using the Monte Carlo simulation toolkit Gate 9.2 ([27]). During the decay of ^{225}Ac , several daughter radionuclides are generated. These daughter radionuclides further decay to granddaughters while generating measurable gamma rays. The decay chain is illustrated in Fig. 1a). Two energy peaks (218 keV, 440 keV) are simulated simultaneously and reconstructed separately in this study. We conducted two sets of simulations. Initially, we

> REPLACE THIS LINE WITH YOUR MANUSCRIPT ID NUMBER (DOUBLE-CLICK HERE TO EDIT) <

placed a Derenzo-like phantom in the center of the FOV, and system parameters were adjusted. We measured spatial resolution as well as sensitivity with the goal of achieving optimal system performance with a single detector. We selected the typical administered dose for prostate cancer targeting PSMA, which is 1.5 mCi. This dose level represents the most widely tested usage among all the completed and ongoing clinical trials. To mitigate the impact of insufficient counts on the reconstructed resolution, the phantom activity was set to 0.84 MBq/cc to ensure a large quantity of detected counts for reconstruction. The length of the phantom used for parameters determination was set to 1 cm. We selected the geometry parameters based on the reconstructed resolution. Once the geometry parameters were chosen, we modified the phantom settings to represent clinically relevant dose levels. Specifically, the phantom activity was set to 0.1MBq/cc, and the length of the phantom was increased to 8 cm. We employed the list mode MLEM reconstruction algorithm as presented in [13] to evaluate the imaging resolution. Geometric sensitivity was determined using the formula proposed in [28], method M1. In the reconstruction process, only the coincidences undergoing Compton scattering followed by a photoelectric absorption are utilized. The simulation settings of the source are presented in section A. The detector design is summarized in section B. The collimator-less SPECT system is detailed in section C.

A. Simulation setting

The central cut of the simulated phantom is shown in Fig. 1b). The gamma photons are simulated to be 218 keV and 440 keV, and the hot region of the Derenzo Phantom contains activity of 0.84 MBq/cc for ^{225}Ac . Considering the branching ratio of 11.4% for ^{221}Fr and 25.9% for ^{213}Bi , the estimated activity is 0.218 MBq/cc at 440 keV and 0.095 MBq/cc at 218 keV. The half-life for ^{221}Fr is simulated to be 4.8 minutes, and a half-life of 45.6 minutes is simulated for ^{213}Bi . The total activity of ^{225}Ac is set to 1.5 mCi, with an acquisition time of 16 minutes. The source comprises hot rods with diameters of 10 mm, 8 mm, 6 mm, 5.5 mm, 4.5 mm and 3.5 mm, each with a length of 1 cm. Positioned 10 cm from the first scatterer in air, the source is reconstructed to optimize detector parameters. Following the selection of detector parameters, the phantom activity is adjusted to 0.1 MBq/cc, and the phantom length is extended to 8 cm. The phantom is moved within the FOV of the whole-body system, and the resolution is measured at different locations for two energy peaks.



a)

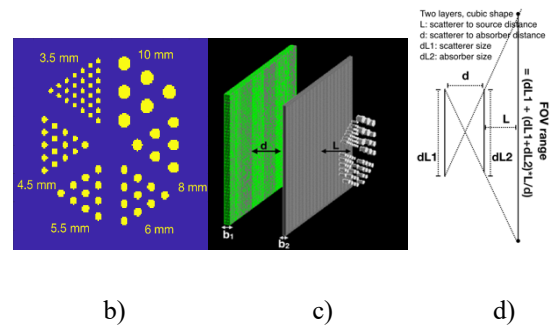


Fig. 1. a) Decay chain of ^{225}Ac , b) central slice of the simulated Derenzo phantom, c) simulation geometry of single detector for parameters optimization with a 1 cm thick phantom, d) illustration of the FOV calculation.

B. Detector design

The goal of this section is to determine the optimal geometry parameters for the detector shown in Fig. 1. The individual camera detector consists of one absorber and several scattering layers, all having the same size on the detector surface but varying in thickness for each interaction layer. An ideal detector material for a Compton camera should exhibit significant Compton scattering (CS) in the scattering layers and efficient photoelectric absorption (PEA) in the absorber, while also maintaining good energy resolution. The likelihood of Compton scattering interaction is proportional to the detector material density, therefore, materials with higher atomic numbers are often preferred for the scatterer. In this study, CZT was chosen for the scatterer due to its atomic number Z of 50, which is higher than that of germanium ($Z=32$). Additionally, CZT offers better achievable energy resolution in existing fabrication processes. The best achievable energy resolution at 122 keV ranges from 2.84% to 3.27% for CZT [29], considering manufacturing constraints, we opted for a simulated energy resolution of 3.1% full width half maximum (FWHM) at 218 keV. In addition to the choice of detector material, energy resolution and detector surface, the following parameters were optimized in the system design to achieve optimal resolution and relatively high sensitivity.

- 1. detector thickness
- 2. distance between scatterer and absorber
- 3. detector pixels dimension

In this study, a fixed 20 cm x 20 cm detector surface is utilized. The parameters mentioned above are investigated individually. Once the geometry parameters are determined, the performance of the collimator-less SPECT system, comprising the optimized detector, is evaluated. Reconstruction is conducted using the list-mode MLEM, with system matrix modeling following the approach proposed in [13]. Only one layer of scattering is simulated. Coincidences are selected within a timing window of 3 ns, and events with multiple interactions within the same detector volume are rejected. Coincidences with total energy deposition within the ranges of 211-225 keV for ^{221}Fr , and 430-

> REPLACE THIS LINE WITH YOUR MANUSCRIPT ID NUMBER (DOUBLE-CLICK HERE TO EDIT) <

450 keV for ^{213}Bi are chosen. With a fixed dose source dose, the impact of three key parameters: the thickness of the scatterer b , the distance from the scatterer to the absorber d , and the detector pixel size p , is evaluated separately. The objective is to define the parameters that can achieve both good sensitivity and imaging resolution with the current reconstruction method implemented. Reconstruction resolution and detected counts are considered as metrics for assessing system performance.

One critical factor influencing Compton imaging quality is the detector energy resolution, which contributes to angular uncertainties of the Compton cone. Various models have been proposed for calculating angular uncertainties based on energy measurements [30]. During the detection of photons, multi-scattering could occur. In this work, the simulated camera consists of two layers, one for scattering and one for photoelectric absorption. Coincidences involving two interactions may include events with multi-scattering. Only coincidences where the total deposited energies falls within an energy window ($E_0 \pm \text{FWHM}$) are used in the reconstruction, with E_0 representing the initial energies of gamma rays. The Compton scattering angle for a coincidence involving only two interactions, first being Compton scattering and second being photoelectric absorption, can be expressed by the following equation:

$$\cos(\beta) = 1 - \frac{m_e c^2 E_1}{E_2(E_1 + E_2)} \quad (1)$$

where E_1, E_2 are the energies deposited in the detector during the first and second interactions, respectively.

The energy detection model used to estimate the resolution of β assumes that the uncertainties of energy detected by the scatterer and absorber both impact the Compton cone. The angular uncertainty δ of the cone cross-section on the plane parallel to the detector at a distance L is approximately calculated by $\delta = \Delta\beta L$. The angular uncertainty model proposed in [30] is applied to calculate $\Delta\beta$ (eq. 2). The simulated energy resolution R at energy E follows inverse square law: $R = R_0 \frac{\sqrt{E_0}}{\sqrt{E}}$, where R_0 corresponds to the energy resolution at energy E_0 .

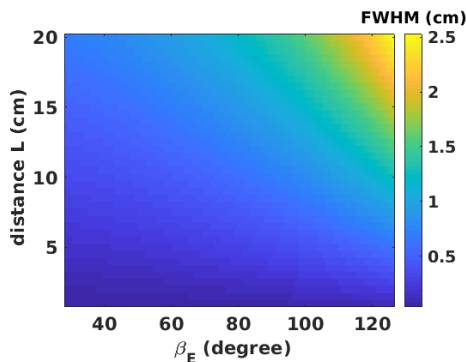


Fig. 2. FWHM @ 218 keV of the uncertainties in the parallel cross-section of the Compton scattering cone, plotted as a function of scattering angle β_E and distance to the detector

plane, β_E represents the Compton scattering angle calculated based on energies.

$$\Delta\beta = \frac{m_e c^2}{(E_1 + E_2)^2 \sin\beta} \sqrt{(\Delta E_1)^2 + (E_1(2E_2 + E_1)\Delta E_2 / E_2^2)^2} \quad (2)$$

Here, E_1, E_2 correspond to the measured energies in scattering and photoelectric absorption, and $\Delta E_1, \Delta E_2$ represent the uncertainties of these measurements. In human whole-body imaging, the FOV is larger compared to small animal imaging, leading to significantly variations in conical shell uncertainties within the FOV, which notably impact on the reconstruction resolution. We plot the achievable FWHM of the conical uncertainties as a function of angular uncertainties and distance to the detector. Fig. 2 illustrates the FWHM of the uncertainties of the cross-section of Compton scattering cone as a function of scattering angle and distance to the detector plane, assuming an energy resolution of 3.1% @ 218 keV for CZT. The energies E_1 and E_2 are supposed to sum up to the photon initial energy (218 keV) in Fig. 2, and the uncertainties of measurements $\Delta E_1, \Delta E_2$ are calculated using the inverse square law. The color-bar represents the FWHM in centimeters. The FWHM of the conical uncertainties ranges from 0.68 cm to 2.53 cm at a distance of 20 cm from the detector, with an average FWHM of 1.29 cm. We will demonstrate in the results section that the actual reconstructed resolution is better than 1.29 cm at a distance of 20 cm.

The absorber is designed to stop the scattered photons, and the thickness (unit in centimeters) required to stop 85% of photons @ energy E is calculated by

$$b = -10 * \ln(1 - 0.85) / (G * k) \quad (3)$$

where k is the material density, which is 5.83 g cc^{-1} for CZT ([31]), and G is the photoelectric absorption coefficient, for an incident photon energy E of approximately 218 keV, G is approximately 0.246 cc g^{-1} , a thickness of absorber larger than 13.2 mm can stop 85% photons. With an absorber thickness equal to 10 mm, as simulated in this study, approximately 76% of photons at 218 keV can be stopped and fully absorbed.

The scatterer thickness should be optimized to maximize the number of photons undergoing only Compton scattering without subsequent photoelectric absorption. When Compton scattering occurs first on the absorber followed by photoelectric absorption in the scattering layer, a backscattering event could be recorded. During photon detection, without involving time-of-flight (TOF) techniques, both scattering and backscattering can occur, resulting in a higher number of detected photons than forward scattering counts. The possibility of Compton scattering and photoelectric absorption depends on the photon energy and material, because the energy changes after the first scattering, we chose to determine the optimized thickness of scatterer through Monte Carlo simulation instead of approximate calculation. A point-like source is simulated separately at 218 keV and 440 keV in air at varying distances from the detector, and sensitivity is calculated as the ratio of

> REPLACE THIS LINE WITH YOUR MANUSCRIPT ID NUMBER (DOUBLE-CLICK HERE TO EDIT) <

detected coincidences to the total emitted counts. It should be noted that this simulated sensitivity is not the same as the geometric sensitivity applied in the reconstruction ([13, 28]). In the reconstruction process, only events that undergo one scattering and one photoelectric absorption within different layers of the detector are classified as Compton coincidences, multi-scattering events are filtered by the energy window, and photons that undergo multiple interactions within the same layer of the detector are also excluded.

An illustration of the FOV calculation is shown in Fig. 1d). Denoting the distance from the scatterer to absorber as d , the size of the cross section of the FOV at a distance L from the detector is calculated as $40 \cdot L/d + 20$ cm, with both the scatterer and absorber each measuring 20 cm. To achieve an FOV size of 40 cm, equivalent to the average human shoulder width, at a distance of 10 cm from the source to the detector (half of the torso size in the sagittal plane), the distance d from the scatterer to the absorber should be less than 20 cm. Three scatterer thickness b_2 of 2 mm, 5 mm, and 10 mm are simulated, along with three scatterer-to-absorber distances d of 10 cm, 15 cm, and 20 cm. Additionally, three detector resolutions are tested: 0.2 mm, 0.5 mm, 1.0 mm for the scatterer, and 0.5 mm, 1.0 mm, 1.5 mm for the absorber. All reconstructed central slices are obtained at the 20th iteration of the reconstruction with a voxel size set to 1 mm^3 .

C. Collimator less SPECT whole-body system

The simulated system consists of 2 detector modules. Each module has 10×10 Cadmium zinc telluride (CZT) blocks, where each block is composed of one layer for photoelectric absorption and one layer for Compton scattering. The absorber layer has 40×40 pixels (each measuring 0.5×0.5 mm) with a thickness of 1 cm. The scattering layer has 100×100 pixels (each measuring 0.2×0.2 mm) with a thickness of 5 mm. The detailed system geometry is illustrated in Fig. 3. Denoting the distance from the first detector to the source as L_1 , and the distance from the second detector to the source as L_2 , the size of the edge of the FOV varies from 84 cm to 141 cm in the coronal plane, with L_1 changing from 10 cm to 20 cm, this configuration provides adequate coverage for human whole-body scanning.

To demonstrate the system's capability to image long-length objects while the detector moves along the patient bed, we simulated a rectangular shape source ($1 \times 1 \times 30$ cm) containing 440 keV photons with activity 5300 Bq/cc along the patient bed. We measured the reconstructed intensity with detector 1 fixed and detector 2 moving along the z-axis from $z = -15$ cm to 15 cm with a 1 cm sampling interval. The rectangular source was positioned at $L_1 = 10$ cm, $L_2 = 12$ cm, and the acquisition time was 30 seconds for each sample. Next, to evaluate the imaging performance at different locations in the FOV, we fixed the two detectors and measured the reconstructed resolution by changing the distance from the detectors to a Derenzo source. The Derenzo source containing ^{225}Ac for two energy peaks (218 keV, 440 keV) was reconstructed to demonstrate prospective imaging performance. The simulated Derenzo phantom, having the transversal slice similar to Fig. 1b but with a length of 8 cm was placed at different distances from the detectors to estimate the reconstructed resolution for whole-body imaging. The

source containing 1.4 mCi ^{225}Ac in total was simulated in air for 16 minutes, with a hot rods activity of 0.1 MBq/cc. The energy resolution of the detector was simulated to be 3.1% @ 218 keV.

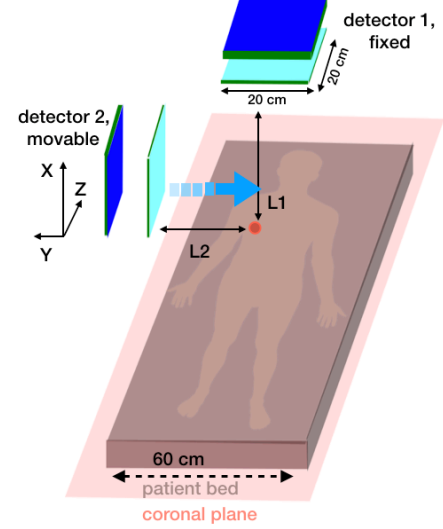


Fig. 3. System illustration: the 2 detectors together cover a whole-body imaging FOV. The red point corresponds to the center of the source, and the blue arrow indicates the direction of movement of detector 2.

III. RESULTS

A. Sensitivity and resolution with Single detector

The simulated sensitivity at a distance of 10 cm to the detector with varying scatterer thicknesses is presented in Fig. 4. The point-like source is simulated separately at 218 keV and 440 keV in air, emitting from a distance of 10 cm from the scatterer. The distance between the scatterer and absorber is fixed at 10 cm, and the absorber thickness is fixed at 10 mm.

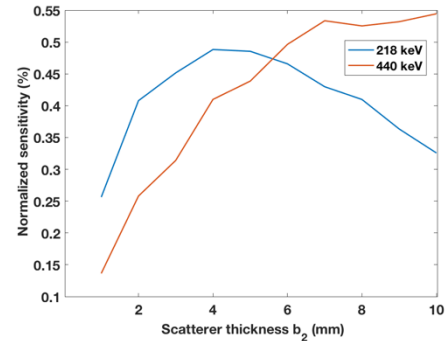


Fig. 4. Simulated sensitivity as a function of scatterer thickness at a distance of 10 cm from the detector.

> REPLACE THIS LINE WITH YOUR MANUSCRIPT ID NUMBER (DOUBLE-CLICK HERE TO EDIT) <

The reconstruction results at the 20th iteration are shown in Fig. 5 and Fig. 6 with varying scatterer-to-absorber distance d and varying scatterer thickness b_2 , in both cases, 4.5 mm rods can be resolved. The sensitivity as a function of coincidence count

applied in the reconstruction for each geometry is summarized in table 2 and table 3. The detector pixel resolution is set to small value (FWHM of 0.2 mm for the scatterer and 0.5 mm for the absorber) to accurately estimate the detection location.

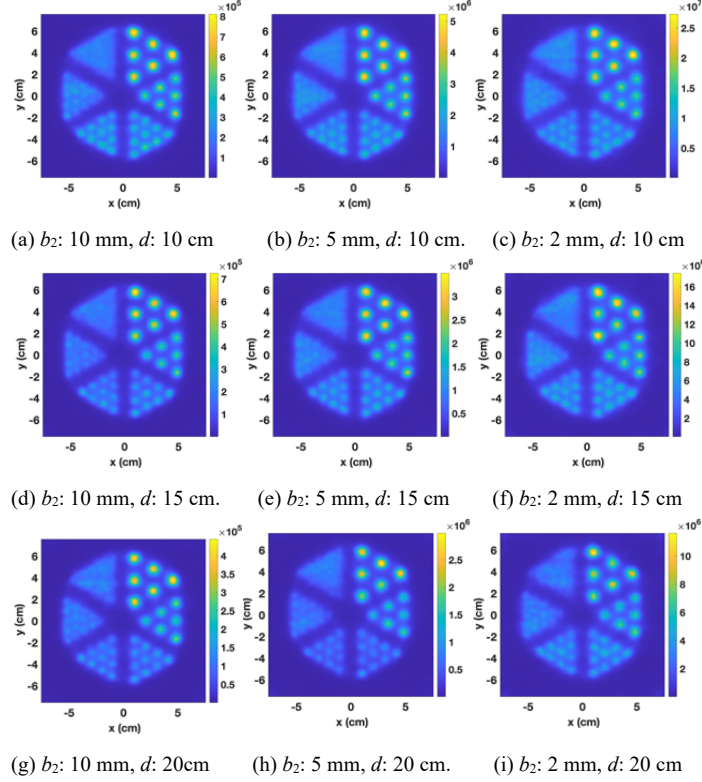


Fig. 5. Reconstruction results at 218 keV with the source placed at 10 cm parallel to the detector plane. Simulations were conducted using three scatterer thicknesses b_2 (2 mm, 5 mm, 10 mm) and three scatterer-to-absorber distances d (10 cm, 15 cm, 20 cm). The reconstructed central slices were obtained at the 20th iteration.

TABLE II

COUNTS USED IN THE RECONSTRUCTION FOR DIFFERENT GEOMETRY PARAMETERS: DETECTOR DISTANCE d AND SCATTERER THICKNESS b_2 , 218 keV SIMULATED.

b_2 \ d	10 mm	5 mm	2 mm
10 cm	1.26M	2.01M	1.76M
15 cm	851K	1.30M	1.08M
20 cm	596K	887K	708K

TABLE III

COUNTS USED IN THE RECONSTRUCTION FOR DIFFERENT GEOMETRY PARAMETERS: DETECTOR DISTANCE d AND SCATTERER THICKNESS b_2 , 440 keV SIMULATED.

b_2 \ d	10 mm	5 mm	2 mm
10 cm	1.84M	1.70M	1.06M
15 cm	1.04M	915K	547K
20 cm	649K	548K	313K

> REPLACE THIS LINE WITH YOUR MANUSCRIPT ID NUMBER (DOUBLE-CLICK HERE TO EDIT) <

Denoting the scatterer pixel resolution as p_1 , absorber pixel resolution as p_2 , the reconstructed resolution at the 20th iteration with varying detector pixel sizes is summarized in

table 4 and table 5. Reconstructed images are shown in Fig.7 and Fig.8. The scatterer-to-absorber distance is fixed at 10 cm, the scatterer thickness is fixed at 5 mm.

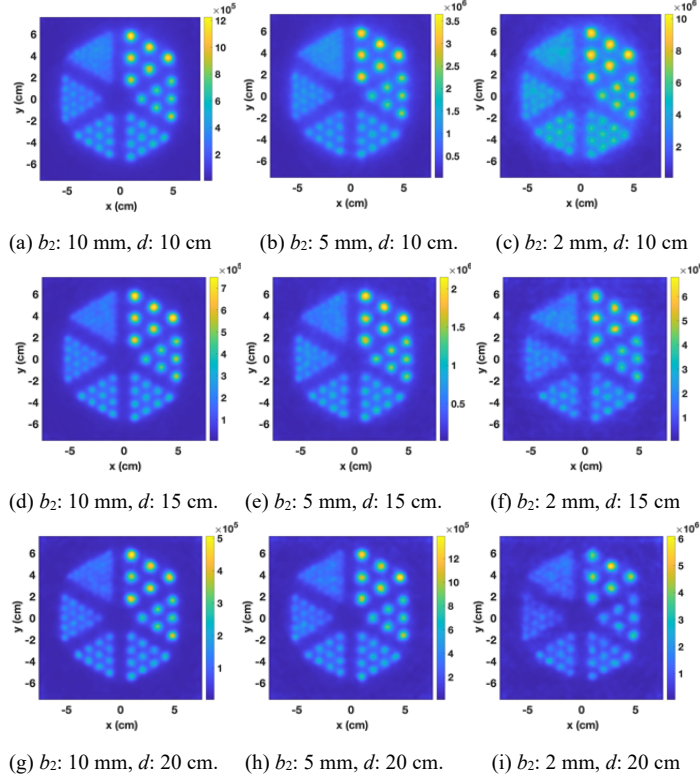


Fig. 6. Reconstruction results at 440 keV with source placed at 10 cm parallel to the detector plane. Simulations were conducted using three scatterer thickness b_2 2 mm, 5 mm, 10 mm, and three scatterer-to-absorber distance d (10 cm, 15 cm, 20 cm). The reconstructed central slices were obtained at the 20th iteration.

TABLE IV

RECONSTRUCTED RESOLUTION WITH DIFFERENT SCATTERER PIXEL SIZE p_1 , ABSORBER PIXEL SIZE p_2 SIMULATED, SCATTERER THICKNESS IS 5 mm, 218 keV SIMULATED.

$p_1 \backslash p_2$	0.5 mm	1.0 mm	1.5 mm
0.2 mm	4.5 mm	4.5 mm	5.5 mm
0.5 mm	4.5 mm	4.5 mm	5.5 mm
1.0 mm	5.5 mm	5.5 mm	5.5 mm

TABLE V

RECONSTRUCTED RESOLUTION WITH DIFFERENT SCATTERER PIXEL SIZE p_1 , ABSORBER PIXEL SIZE p_2 SIMULATED, SCATTERER THICKNESS IS 5 mm, 440 keV SIMULATED.

$p_1 \backslash p_2$	0.5 mm	1.0 mm	1.5 mm
0.2 mm	4.5 mm	4.5 mm	4.5 mm
0.5 mm	4.5 mm	4.5 mm	5.5 mm
1.0 mm	5.5 mm	5.5 mm	5.5 mm

> REPLACE THIS LINE WITH YOUR MANUSCRIPT ID NUMBER (DOUBLE-CLICK HERE TO EDIT) <

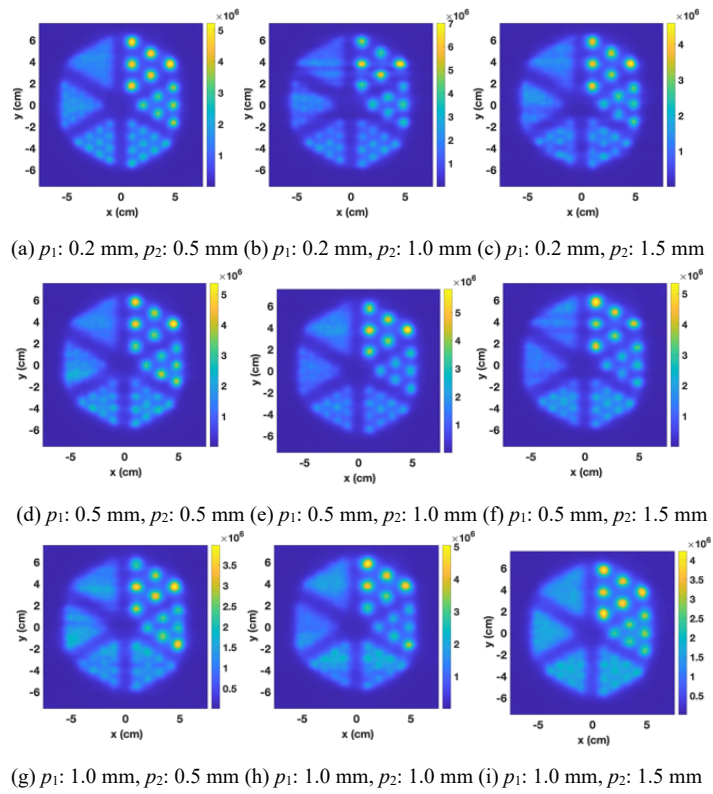
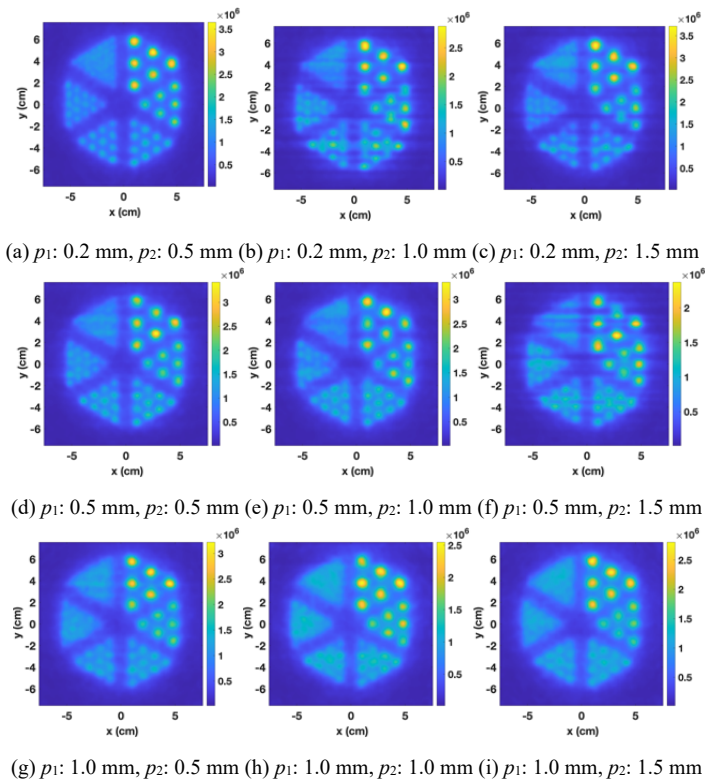


Fig. 7. Reconstruction results at 218 keV with source placed at 10 cm parallel to the detector plane. Three scatterer pixel resolution p_1 0.2 mm, 0.5 mm, 1 mm were simulated. Three absorber pixel resolution p_2 0.5 mm, 1 mm, 1.5 mm were simulated. The reconstructed central slices were obtained at the 20th iteration. The scatterer thickness was 5 mm, the scatterer-to-absorber distance was 10 cm.



> REPLACE THIS LINE WITH YOUR MANUSCRIPT ID NUMBER (DOUBLE-CLICK HERE TO EDIT) <

Fig. 8. Reconstruction results at 440 keV with source placed at 10 cm parallel to the detector plane. Three scatterer pixel resolution p_1 0.2 mm, 0.5 mm, 1 mm were simulated. Three absorber pixel resolution p_2 0.5 mm, 1 mm, 1.5 mm were simulated. The reconstructed central slices were obtained at 20th iteration. The scatterer thickness was 5 mm, the scatterer-to-absorber distance was 10 cm.

B. Reconstruction of whole-body system

The reconstruction of the rectangular-shaped source ($1 \times 1 \times 30$ cm) along the patient bed is shown in Fig. 9a), and the line profile is shown in Fig. 9 b).

Reconstructed results of the whole-body system at 218 keV and 440 keV are shown in Fig. 10 and Fig. 11. In the reconstruction, only the photons undergoing one Compton scattering and one photoelectric absorption are used, backscattering events are not filtered. The reconstructed results with a mixture of 218 keV and 440 keV are shown in Fig. 12.

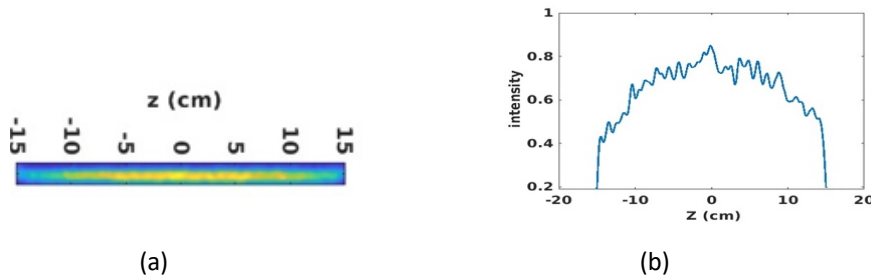


Fig. 9. Reconstructed line source (a) and the line profile (b) at first iteration with detector 2 moving along z-axis. The z-coordinate ranges from -15 cm to 15 cm with a 1 cm sampling interval, and each position is acquired for 30 seconds.

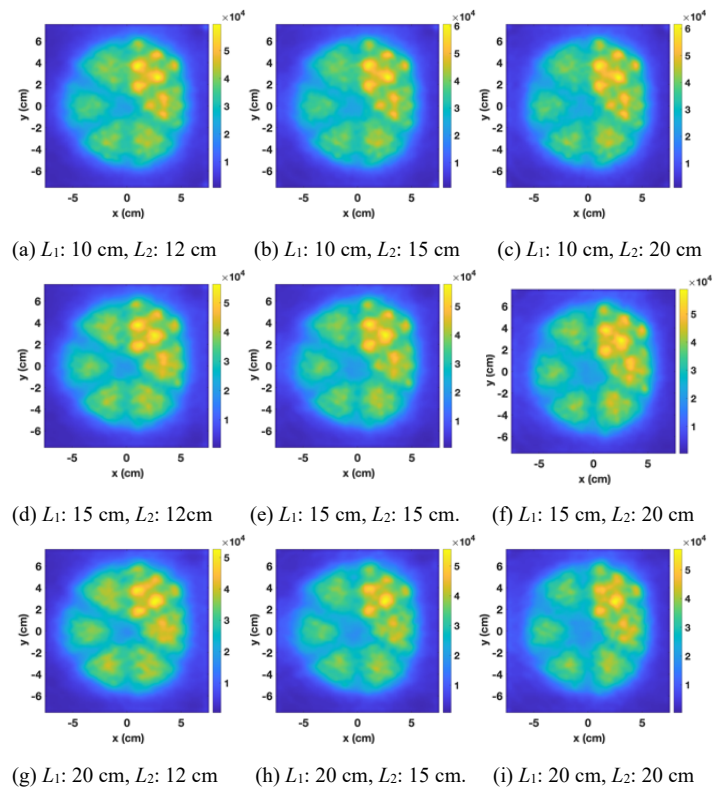


Fig. 10. Reconstruction results at 218 keV.

> REPLACE THIS LINE WITH YOUR MANUSCRIPT ID NUMBER (DOUBLE-CLICK HERE TO EDIT) <

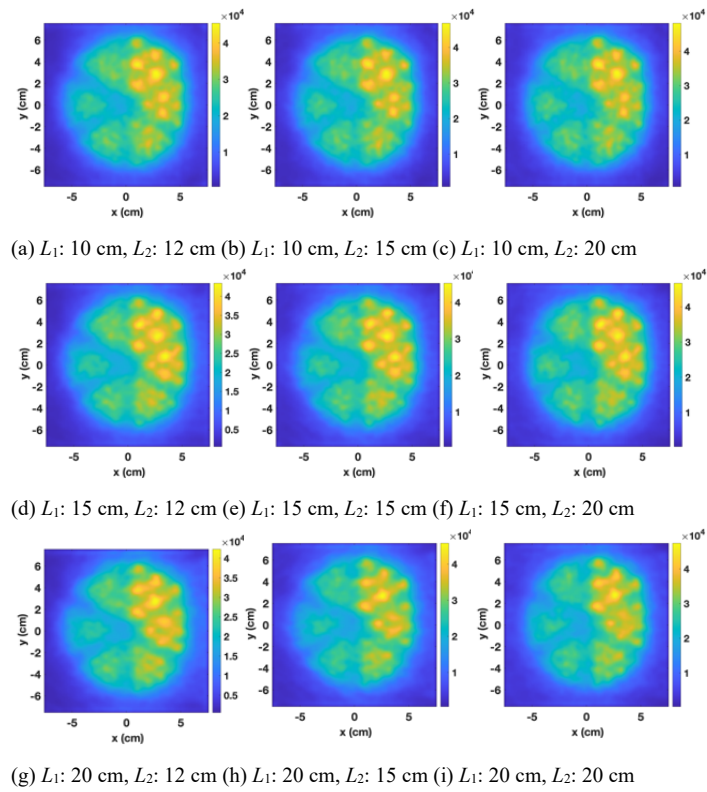


Fig. 11. Reconstruction results at 440 keV.

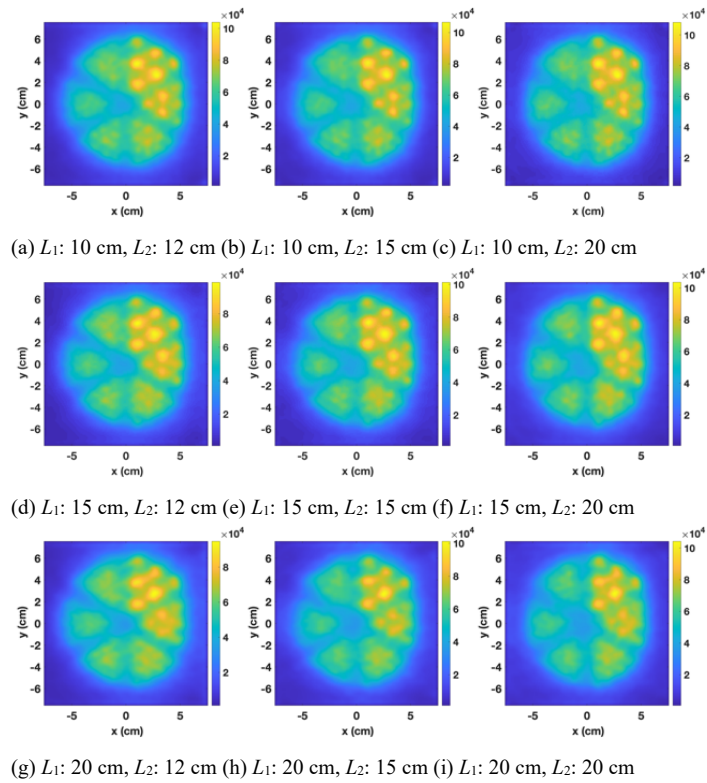


Fig. 12. Reconstruction results with 218 keV and 440 keV reconstructed simultaneously.

IV. DISCUSSION

The results indicate that the scanning time of the collimator-less SPECT system is reduced compared to traditional SPECT, while the potential range of detectable gamma ray energies is expanded compared to PET. The resolution for human whole-body imaging with clinically relevant phantom activity (0.1 MBq/cc) is approximately 1.0 cm with the current reconstruction method. The resolution surpasses that of current SPECT scanners typically used for whole-body applications, which usually have a resolution of 12-16 mm [8].

The impact of the detector parameters on the reconstructed resolution was investigated in this study. For the single detector, several parameters were simulated, including scatterer-to-absorber distance, scatterer thickness, and scatterer and absorber pixel sizes. The optimized parameters were selected based on achieving the best possible imaging resolution with the current system matrix modeling used in the reconstruction. It was observed that when the scatterer pixel size is less than 1.0 mm, reconstructions with absorber pixel sizes larger than 0.5 mm exhibit stripe artifacts. These artifacts decrease when using scatterer pixel sizes greater than 1.0 mm and absorber pixel sizes larger than 1.5 mm. However, a larger detector pixel size results in reduced imaging resolution, ranging from 4.5 mm to 5.5 mm. Selecting the scatterer thickness requires a delicate balance. A smaller thickness results in fewer detected photons, whereas a larger thickness can stop the photons, leading to multiple interactions on the same scatterer that cannot be used in the reconstruction process. A scatterer thickness of 5 mm was chosen based on Monte Carlo simulation, although a precise mathematical calculation for determining the optimal scatterer thickness has not been established yet. In the future, we will propose a model for calculating the probability of a photon being detected as a reconstructable coincidence, involving Compton scattering followed by photoelectric absorption.

For the two-detector system designed for human whole-body imaging, based on the reconstructed results of a single detector, the following parameters were chosen: a scatterer-to-absorber distance of 10 cm, a scatterer thickness of 5 mm, a scatterer pixel size of 0.2 mm, and an absorber pixel size of 0.5 mm. The reconstructed image of the line source has demonstrated homogeneity in the center along the patient bed with one fixed detector and one moving detector, showcasing the feasibility of imaging a large area in a short time (16 minutes). However, the reconstructed line exhibits non-uniformity at the end of the patient bed, mainly caused by the mismatch between the system sensitivity of a moving detector and the geometric sensitivity calculated with a fixed detector applied in the reconstruction. Regarding the reconstruction results obtained with the Derenzo source, images shown in Fig. 10 at the energy peak of 218 keV appear to be blurred compared to Fig. 11 at 440 keV. This blurring is expected because Compton imaging performs better at higher energy. Additionally, for 218 keV photons, the energy uncertainties caused by Doppler broadening are larger than those at 440 keV, which ultimately leads to lower image quality.

The results demonstrate that with a source activity of 0.84 MBq/cc, a resolution of 4.5 mm can be achieved at a distance of 10 cm from the detector. With a reduced source activity of

0.1 MBq/cc, the achievable resolution is 1 cm. Over the past twenty years, studies have successfully demonstrated the feasibility of small animal imaging using the Compton camera modality. However, the potential for human whole-body imaging remains uncertain, and no research has yet shown a reconstruction resolution under 1 cm. As targeted alpha therapy is a novel therapeutic approach under investigation, there exists no standard protocol for resolution measurement. Various studies have simulated different dosages. A CZT-based small animal imaging system with enhancing sensitivity was proposed in [3]. The authors simulated a smaller Derenzo phantom with activities of 4 μ Ci and 1 μ Ci for 15 minutes in air, the phantom activities were measured at 1.97 MBq/cc and 0.49 MBq/cc, respectively, achieving a best achievable resolution of 2 mm. A GAGG-based Compton camera for small animal imaging was presented in [32], where the authors simulated hot rods with activities ranging from 3 to 8 MBq/cc in water. For evaluating the performance of our whole-body system, we simulated a lower dosage intensity (0.1 MBq/cc) to demonstrate image resolution comparable to clinical applications. Future work will involve incorporating a warm background and investigating the effects of hot region intensity on the reconstructed images.

While Compton cameras excel in imaging high-energy gamma rays, their primary application in human imaging seems to be in proton therapy monitoring. Nevertheless, our study indicates that for localized tumors or for a smaller FOV, Compton cameras offer advantages in multi-isotope imaging and greater sensitivity compared to mechanically collimated SPECT. We believe that the achievable imaging resolution of 1 cm for lower doses (0.1 MBq/cc) can be improved through refined event selection and modeling in the reconstruction process. All the reconstructions were performed using the system matrix proposed in [13] and the sensitivity matrix proposed in [28]. Although previous studies have demonstrated agreement between the calculated sensitivity and simulated sensitivity, a comparison of the system matrix with the simulation is still needed. Evaluation of the system's imaging performance by reconstructing imaged using a Monte Carlo simulated system matrix will be done in future work.

This work has several limitations related to the simulation of TAT monitoring using CC system. The first is that, for the chosen radionuclide Actinium (Ac), only two energy peaks are simulated and reconstructed. Other photon emitters such as ^{213}Po and ^{217}At are not simulated in this study, although they would contribute to random detections. A more comprehensive simulation of gamma emitters, as well as random and scatter events, should be conducted to further evaluate the imaging performance of the proposed system. Additionally, the two energy peaks are simulated separately. Down-scattering caused by 440 keV scattered photons is not simulated and will be investigated in future work. Only Actinium is used in this study, and the gamma energy generated in TAT can range from 117 keV to 893 keV, depending on the alpha emitters. Higher energy photons will introduce randoms during the detection of gamma rays. We only evaluated Actinium because it is the most widely used agent for TAT, but more investigation is needed to assess the capability of imaging multi-energetic gamma rays generated from other existing alpha emitters, such as ^{211}At or

^{227}Th . The background environment is simulated as air, while water should resemble the human body more closely for evaluating a whole-body system. Another limitation is the event selection methods. We only select the coincidences that have two interactions, first Compton scattering and second photoelectric absorption for the two interactions, and the sum of the deposited energy for the incident gamma photon within an energy window. This selection limits the counts used in the reconstruction, even though the total detected counts are nearly 4 times larger than the counts used, which in turn diminishes one of the advantages of the Compton camera: its higher sensitivity compared to collimated SPECT. To increase the usable counts in the reconstruction, new algorithms including an event selection model and a new system matrix model adapted to multi-interaction coincidences will be developed in future work. Spectrum deconvolution should be considered to reduce the noises of the input. Machine learning methods, such as neural networks, might help increase the signal to background ratio ([33]). Multi-scattering layers should also be simulated and compared to the current single scatterer system to increase sensitivity. Moreover, for ^{225}Ac , the two major gamma rays (218 keV, 440 keV) generated from ^{221}Fr and ^{213}Bi are easy to separate, the system's performance needs to be investigated, especially for gammas having close energy levels. Backscattering events are considered in the reconstruction, contributing to blurring in the reconstructed images. The addition of TOF information might enhance resolution by allowing the filtering of backscattering events. Furthermore, the current system has a planar shape, varying distances between the scatterer pixels and absorber pixels, or even a spherical-shaped detector, might improve the imaging resolution and sensitivity, which requires further geometric design.

V. CONCLUSION

We demonstrated the feasibility of Compton camera imaging for whole-body applications during TAT treatment. We simulated a Derenzo phantom, containing a clinically relevant dose, within a field of view suitable for whole-body human imaging. The reconstructed resolution was measured at various source locations using the current detector design. Using a total activity of 1.5 mCi of ^{225}Ac (0.84 MBq/cc), the best achievable resolution at 10 cm from the detector is 4.5 mm, with an energy resolution of 3.1% FWHM at 218 keV. An 8 mm spatial resolution is achieved with the source placed 20 cm from the detector. For simulated source activity closer to clinical usage (0.1 MBq/cc), the resolution decreases, and only 1 cm rods can be resolved with an acquisition time of 16 minutes. The current whole-body system design is suitable for fast scanning when high imaging resolution is not necessary. Although the imaging resolution of the whole-body system does not surpass that demonstrated in other studies for small animal imaging, it presents a potential solution for dynamic whole-body imaging of TAT agent. It's important to note that the current evaluation only considers two plate detectors; ongoing improvements in system geometry will be conducted. Further evaluation of imaging performance will involve moving detector 2 along the patient bed when simulating a body phantom.

REFERENCES

- [1] Todd, R.W., J. Nightingale, and D. Everett, *A proposed γ camera*. *Nature*, 1974. **251**(5471): p. 132-134.
- [2] Nurdan, T.C., et al., *Design criteria for a high energy Compton camera and possible application to targeted cancer therapy*. *Journal of Instrumentation*, 2015. **10**(07): p. C07018.
- [3] Caravaca, J., et al., *Compton and Proximity Imaging of Ac In Vivo With a CZT Gamma Camera: A Proof of Principle With Simulations*. *IEEE Transactions on Radiation and Plasma Medical Sciences*, 2022. **6**(8): p. 904-915.
- [4] Börjesson, P.K., et al., *Performance of immuno-positron emission tomography with zirconium-89-labeled chimeric monoclonal antibody U36 in the detection of lymph node metastases in head and neck cancer patients*. *Clinical Cancer Research*, 2006. **12**(7): p. 2133-2140.
- [5] Knight, J.C., et al., *Dual-isotope imaging allows in vivo immunohistochemistry using radiolabelled antibodies in tumours*. *Nuclear Medicine and Biology*, 2019. **70**: p. 14-22.
- [6] Kręcis, P., et al., *Radiolabeled peptides and antibodies in medicine*. *Bioconjugate Chemistry*, 2020. **32**(1): p. 25-42.
- [7] Huh, Y., et al., *Simulation studies of a full-ring, CZT SPECT system for whole-body imaging of ^{99m}Tc and ^{177}Lu* . *Medical Physics*, 2023.
- [8] Hutton, B.F., *SPECT imaging: Basics and new trends*, in *Handbook of Particle Detection and Imaging*. 2021, Springer. p. 1217-1236.
- [9] Hijnen, N.M., et al., *Dual-isotope $^{111}\text{In}/^{177}\text{Lu}$ SPECT imaging as a tool in molecular imaging tracer design*. *Contrast Media & Molecular Imaging*, 2012. **7**(2): p. 214-222.
- [10] Nakano, T., et al., *Imaging of ^{99m}Tc -DMSA and ^{18}F -FDG in humans using a Si/CdTe Compton camera*. *Physics in Medicine & Biology*, 2020. **65**(5): p. 05LT01.
- [11] Koyama, A., et al., *Prototype of a single probe Compton camera for laparoscopic surgery*. *Nuclear Instruments and Methods in Physics Research Section A: Accelerators, Spectrometers, Detectors and Associated Equipment*, 2017. **845**: p. 660-663.
- [12] Yoshida, E., et al., *Whole gamma imaging: a new concept of PET combined with Compton imaging*. *Physics in Medicine & Biology*, 2020. **65**(12): p. 125013.
- [13] Maxim, V., et al., *Probabilistic models and numerical calculation of system matrix and sensitivity in list-mode MLEM 3D reconstruction of Compton camera images*. *Physics in Medicine & Biology*, 2015. **61**(1): p. 243.
- [14] Muñoz, E., et al., *Study and comparison of different sensitivity models for a two-plane Compton camera*. *Physics in Medicine & Biology*, 2018. **63**(13): p. 135004.
- [15] Klutz, P.G., et al., *Radium Ra 223 dichloride injection: US Food and Drug Administration drug approval summary*. *Clinical cancer research*, 2014. **20**(1): p. 9-14.
- [16] Seo, Y., *Quantitative imaging of alpha-emitting therapeutic radiopharmaceuticals*. *Nuclear medicine and molecular imaging*, 2019. **53**(3): p. 182-188.
- [17] Jang, A., et al., *Targeted alpha-particle therapy: a review of current trials*. *International journal of molecular sciences*, 2023. **24**(14): p. 11626.
- [18] Suliman, G., et al., *Half-lives of ^{221}Fr , ^{217}At , ^{213}Bi , ^{213}Po and ^{209}Pb from the ^{225}Ac decay series*. *Applied Radiation and Isotopes*, 2013. **77**: p. 32-37.
- [19] Ocak, M., et al., *Post-therapy imaging of ^{225}Ac -DOTATATE treatment in a patient with recurrent neuroendocrine tumor*. *European Journal of Nuclear Medicine and Molecular Imaging*, 2020. **47**(11): p. 2711-2712.
- [20] Kamaleshwaran, K.K., et al., *Whole-body and single-photon emission computed tomography/computed tomography postpeptide receptor alpha radionuclide therapy images of actinium 225-tetraazacyclododecanetetraacetic acid-octreotide as a primary modality of treatment in a patient with advanced rectal neuroendocrine tumor with metastases*. *Indian Journal of Nuclear Medicine*, 2020. **35**(3): p. 226-228.

> REPLACE THIS LINE WITH YOUR MANUSCRIPT ID NUMBER (DOUBLE-CLICK HERE TO EDIT) <

- [21] Królicki, L., et al., *Dose escalation study of targeted alpha therapy with [225 Ac] Ac-DOTA-substance P in recurrence glioblastoma—safety and efficacy*. European Journal of Nuclear Medicine and Molecular Imaging, 2021. **48**: p. 3595-3605.
- [22] Vatsa, R., et al., *225Ac-PSMA-617 radioligand posttherapy imaging in metastatic castrate-resistant prostate cancer patient using 3 photopeaks*. Clinical Nuclear Medicine, 2020. **45**(6): p. 437-438.
- [23] Atallah, E.L., et al., *A phase 2 study of actinium-225 (225Ac)-lintuzumab in older patients with untreated acute myeloid leukemia (AML)-interim analysis of 1.5 μ Ci/kg/dose*. Blood, 2018. **132**: p. 1457.
- [24] Uenomachi, M., et al., *Double photon emission coincidence imaging with GAGG-SiPM Compton camera*. Nuclear Instruments and Methods in Physics Research Section A: Accelerators, Spectrometers, Detectors and Associated Equipment, 2020. **954**: p. 161682.
- [25] Llosá, G. and M. Rafecas, *Hybrid PET/Compton-camera imaging: an imager for the next generation*. The European Physical Journal Plus, 2023. **138**(3): p. 214.
- [26] Benabdallah, N., et al., *Practical considerations for quantitative clinical SPECT/CT imaging of alpha particle emitting radioisotopes*. Theranostics, 2021. **11**(20): p. 9721.
- [27] Etxebeste, A., et al., *CCMod: a GATE module for Compton camera imaging simulation*. Physics in Medicine & Biology, 2020. **65**(5): p. 055004.
- [28] Feng, Y., et al., *Influence of Doppler broadening model accuracy in Compton camera list-mode MLEM reconstruction*. Inverse Problems in Science and Engineering, 2021. **29**(13): p. 3509-3529.
- [29] Chun, S.-D., et al., *Property of a CZT semiconductor detector for radionuclide identification*. Journal of Nuclear Science and Technology, 2008. **45**(sup5): p. 421-424.
- [30] Ordonez, C.E., A. Bolozdynya, and W. Chang. *Dependence of angular uncertainties on the energy resolution of Compton cameras*. in 1997 IEEE Nuclear Science Symposium Conference Record. 1997. IEEE.
- [31] Diéguez, E., *Growth of Cd0.9Zn0.1Te bulk crystals*. 2011.
- [32] Yoon, C., et al., *Estimate of the 225 Ac radioactive isotope distribution by means of DOI compton imaging in targeted alpha radiotherapy: A Monte Carlo simulation*. Journal of the Korean Physical Society, 2020. **76**: p. 954-960.
- [33] Munoz, E., et al., *Proton range verification with MACACO II Compton camera enhanced by a neural network for event selection*. Scientific reports, 2021. **11**(1): p. 9325.